

Coherent manipulation of a tunable hybrid qubit via microwave control

Si-Si Gu(顾思思), Bao-Chuan Wang(王保传), Hai-Ou Li(李海欧), Gang Cao(曹刚), and Guo-Ping Guo(郭国平)
Citation: Chin. Phys. B, 2023, 32 (**8**): 087302. DOI: 10.1088/1674-1056/acd0a7
Journal homepage: http://cpb.iphy.ac.cn; http://iopscience.iop.org/cpb

What follows is a list of articles you may be interested in

Nonlinear optical rectification of GaAs/$Ga_{1-x}Al_xAs$ quantum dots with Hulthén plus Hellmann confining potential

Yi-Ming Duan(段一名) and Xue-Chao Li(李学超)
Chin. Phys. B, 2023, 32 (**1**): 017303. DOI: 10.1088/1674-1056/ac70bf

Pure spin-current diode based on interacting quantum dot tunneling junction

Zhengzhong Zhang(张正中), Min Yu(余敏), Rui Bo(薄锐), Chao Wang(王超), and Hao Liu(刘昊)
Chin. Phys. B, 2021, 30 (**11**): 117305. DOI: 10.1088/1674-1056/abfbd8

Pure spin-current diode based on interacting quantum dot tunneling junction

Zhengzhong Zhang(张正中), Min Yu(余敏), Rui Bo(薄锐), Chao Wang(王超), and Hao Liu(刘昊)
Chin. Phys. B, 2021, 30 (**11**): 117305. DOI: 10.1088/1674-1056/abfbd8

Optical anisotropy and the direction of polarization of exciton emissions in a semiconductor quantum dot:Effect of heavy- and light-hole mixing

Ranber Singh, Rajiv Kumar, Vikramjeet Singh
Chin. Phys. B, 2017, 26 (**8**): 087303. DOI: 10.1088/1674-1056/26/8/087303

Heat generation by spin-polarized current in a quantum dot connected to spin battery and ferromagnetic lead

Bai Xu-Fang (白絮芳), Sun Lian-Liang (孙连亮), Chi Feng (迟锋)
Chin. Phys. B, 2015, 24 (**5**): 057302. DOI: 10.1088/1674-1056/24/5/057302

Coherent manipulation of a tunable hybrid qubit via microwave control

Si-Si Gu(顾思思)[1,2], Bao-Chuan Wang(王保传)[1,2], Hai-Ou Li(李海欧)[1,2], Gang Cao(曹刚)[1,2,†], and Guo-Ping Guo(郭国平)[1,2,3]

[1] *CAS Key Laboratory of Quantum Information, University of Science and Technology of China, Hefei* 230026, *China*
[2] *CAS Center For Excellence in Quantum Information and Quantum Physics, University of Science and Technology of China, Hefei* 230026, *China*
[3] *Origin Quantum Computing Company Limited, Hefei* 230026, *China*

(Received 23 March 2023; revised manuscript received 25 April 2023; accepted manuscript online 27 April 2023)

Hybrid qubits enable the hybridization of charge and spin degrees of freedom, which provides a way to realize both a relatively long coherence time and rapid qubit manipulation. Here, we use microwave driving to demonstrate the coherent operation of a tunable hybrid qubit, including X-rotation, Z-rotation, and rotation around an arbitrary axis in the X–Y panel of the Bloch sphere. Moreover, the coherence properties of the qubit and its tunability are studied. The measured coherence time of the X-rotation reaches ~ 14.3 ns. While for the Z-rotation, the maximum decoherence time is ~ 5.8 ns due to the larger sensitivity to noise. By employing the Hahn echo sequence to mitigate the influence of the low-frequency noise, we have improved the qubit coherence time from ~ 5.8 ns to ~ 15.0 ns. Our results contribute to a further understanding of the hybrid qubit and a step towards achieving high-fidelity qubit gates in the hybrid qubit.

Keywords: semiconductor quantum dot, hybrid qubit, qubit operation, microwave control

PACS: 73.21.La, 85.35.Be, 03.67.Lx, 42.50.Wk **DOI:** 10.1088/1674-1056/acd0a7

1. Introduction

Qubit hosted on semiconductor quantum dots is a promising candidate for quantum computation due to its scalability and compatibility with industrial manufacturing technologies.[1–6] Over the past decades, different degrees of freedom of electrons in semiconductors have been explored to form qubits. Spin qubits encoded on the spin degree of freedom have long coherence times because they are relatively isolated from the environment. However, such isolation also makes spin qubits face a challenge in realizing fast qubit operations.[1,2,5,7–10] In contrast, charge qubits utilizing the spatial distribution of electrons have advantages in manipulating speed, but they suffer from charge noise and thus dephase rapidly.[11–17] In this context, hybrid qubit has been proposed and investigated extensively (see Table A1 in Appendix A for experimental progress), which combines the longevity of spin qubits and the fast manipulations of charge qubits.[2,18–29]

The hybrid qubit is encoded by the two lowest energy states of three or five electron spins in a double quantum dot (DQD), hybridizing the degrees of freedom of charge and spin.[20–22,24,29] By virtue of the asymmetry and anharmonicity of the confinement potential, a unique tunable hybrid qubit has been demonstrated.[24] The tunability of the hybrid qubit has been well modeled by its quasiparallel energy levels, which enables flexible qubit operations and provides a path to optimize the operation point.[24] Microwave driving is beneficial in realizing precise and reliable qubit manipulation. It allows control of the rotation axis by the microwave phase and operation speed by the microwave amplitude.[16,30] Importantly, it enables the qubit to keep at the optimal working point.[16,23,30] Recently, the operation fidelity of the typical hybrid qubit has been improved via microwave control.[22,29]

In this work, we study the tunability and realize coherent single-qubit manipulations of a tunable hybrid qubit with microwave driving. The tunability of energy levels is investigated by performing microwave spectroscopy. Then we implement X-rotation with the operation speed controlled by the microwave amplitude. In the Ramsey fringe experiment, we demonstrate Z-rotation and optimize the qubit decoherence rate by detuning. Moreover, rotation around an arbitrary axis in the X–Y plane is achieved by leveraging the controllability of the microwave phase. Furthermore, we utilize the Hahn echo sequence to reduce the influence of the low-frequency noise on the qubit. The qubit coherence time is improved to ~ 15.0 ns, which is a factor of approximately 2.6 compared to the maximum coherence time ~ 5.8 ns measured in the Ramsey fringe experiment.

2. Experimental setup

The DQD we studied is defined on a GaAs/AlGaAs heterostructure with metallic electrodes D1–D5 and H1–H2 (Fig. 1(a)). The gate electrodes Q1–Q3 can form a quantum point contact (QPC). As the QPC is capacitively coupled to the DQD,[31] we can obtain the charge states of the DQD by measuring the transconductance of the QPC, $\mathrm{d}I/\mathrm{d}V_{\mathrm{D5}}$. Figure 1(b) shows the charge stability diagram of the DQD obtained by measuring $\mathrm{d}I/\mathrm{d}V_{\mathrm{D5}}$ as a function of gate electrode voltages V_{D1} and V_{D5}. In the figure, (n,m) denotes the electron num-

†Corresponding author. E-mail: gcao@ustc.edu.cn

© 2023 Chinese Physical Society and IOP Publishing Ltd

bers in the left and right dots. We focus on the $(2,3) \leftrightarrow (1,4)$ charge transition, which is indicated by the black circle. Since the two core electrons in the right dot can be neglected when considering the dynamics of the hybrid qubit,[24,25,32] we use the three-electron model to describe our system.

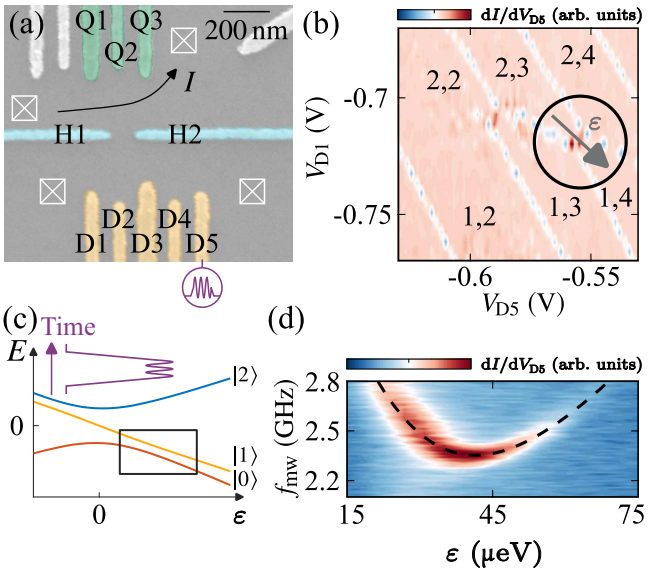


Fig. 1. (a) False-color scanning electron micrograph of the device. The device consists of a DQD (yellow) and a QPC (green). The horizontal electrodes H1 and H2 (blue) are used to control the interaction between the two parts. (b) The charge stability diagram obtained by measuring the QPC's transconductance $\mathrm{d}I/\mathrm{d}V_{\mathrm{D5}}$. We perform the experiment in the area indicated by the black circle. (c) Schematic diagram of the energy level structure as a function of ε, which is calculated with Eq. (1). The purple line depicts the applied pulse sequence. The red, orange and blue lines correspond to the states $|0\rangle$, $|1\rangle$, and $|2\rangle$, respectively. (d) The measured $\mathrm{d}I/\mathrm{d}V_{\mathrm{D5}}$ as a function of detuning ε and microwave frequency f_{mw}. The black dashed line represents the frequency difference between $|0\rangle$ and $|1\rangle$, which is calculated with Eq. (1) using $\Delta_1 = 13$ μeV, $\Delta_2 = 14.3$ μeV, $\delta = -0.1$ μeV and $k = 1.3$. The measured spectrum corresponds to the black rectangle in panel (c).

The hybrid qubit is encoded on the states $|0\rangle = |\uparrow\rangle_{\mathrm{L}}|S\rangle_{\mathrm{R}}$ and $|1\rangle = \sqrt{1/3}|\uparrow\rangle_{\mathrm{L}}|T_0\rangle_{\mathrm{R}} - \sqrt{2/3}|\downarrow\rangle_{\mathrm{L}}|T_+\rangle_{\mathrm{R}}$, where the subscripts R and L indicate that electrons are in the right dot and the left dot, respectively. $|\uparrow\rangle$ and $|\downarrow\rangle$ represent the spin configurations of a single electron, and $|S\rangle$ ($|T_{0,+}\rangle$) is the singlet (triplet) state of two electrons. The third relevant state is $|2\rangle = |S\rangle_{\mathrm{L}}|\uparrow\rangle_{\mathrm{R}}$, which couples to both $|0\rangle$ and $|1\rangle$ and enables electrical control. In the basis of $\{|0\rangle, |1\rangle, |2\rangle\}$, the dynamics of the hybrid qubit system can be described by[24]

$$\boldsymbol{H} = \begin{pmatrix} -\varepsilon/2 & 0 & \Delta_1 \\ 0 & -k\varepsilon/2+\delta & \Delta_2 \\ \Delta_1 & \Delta_2 & \varepsilon/2 \end{pmatrix}, \tag{1}$$

where ε is the energy detuning between the two dots, which is adjusted by the gate voltage V_{D5}. Δ_1 (Δ_2) is the tunnel coupling between $|0\rangle$ and $|1\rangle$ ($|1\rangle$ and $|2\rangle$). Particularly, k derives from the asymmetry and anharmonicity of the potential, which makes the energy levels of the hybrid qubit at positive ε tunable.[24] This is illustrated by the calculated energy levels shown in Fig. 1(c), the two lowest energy levels are not strictly parallel but quasiparallel at large positive ε, different from the original hybrid qubit.[21,22] This quasiparallelism of the energy levels makes the qubit properties adjustable and leads to resistance against noise to a certain extent.[24]

In the following experiments, we initialize the qubit in state $|0\rangle$ using an adiabatic pulse, where ε is changed from negative to positive slowly relative to Δ_1 and Δ_2 as illustrated by the purple line in Fig. 1(c). The qubit states $|0\rangle$ and $|1\rangle$ are mapped into different charge configurations by adiabatically pulsing the system back to the negative ε region,[7,21] which allows for state readout via QPC. More details can be found in our previous work.[24]

By applying a microwave with a frequency f_{mw} to gate D5 and scanning over ε, we perform microwave spectroscopy to characterize the transition frequency f_{q} of the hybrid qubit system. f_{q} is determined by the splitting between the two lowest energy levels, i.e., $f_{\mathrm{q}} = (E_1 - E_0)/h$, where h is Planck constant and E_i is the eigenenergy of state $|i\rangle$. The qubit is excited from its initial state $|0\rangle$ to $|1\rangle$ when $f_{\mathrm{q}} = f_{\mathrm{mw}}$, yielding a resonant peak in the QPC transconductance. The measured transconductance $\mathrm{d}I/\mathrm{d}V_{\mathrm{D5}}$ as a function of ε and f_{mw} is presented in Fig. 1(d), which maps out the energy dispersion and suggests that f_{q} can be tuned with ε. By choosing appropriate parameters, the black dashed curve calculated from Eq. (1) agrees well with the resonant peaks. We find that f_{q} reaches its minimum at $\varepsilon = 41.5$ μeV, which means $|\partial f_{\mathrm{q}}/\partial\varepsilon| = 0$. Moreover, $|\partial f_{\mathrm{q}}/\partial\varepsilon|$ keeps small in a wide range around $\varepsilon = 41.5$ μeV as a consequence of the quasiparallel energy levels, where the qubit is insusceptible to noise and the coherence time can be prolonged.[12,26,33] Hence, this area is denoted as an extended sweet spot.

3. Coherent single qubit operation

We have gained a basic understanding of the energy levels of the qubit in the preceding measurement. Based on this, we now use microwave driving to demonstrate the coherent operation of the hybrid qubit and investigate its coherence performance around the extended sweet spot.

We apply the same microwave pulse sequence in Fig. 1(c) but keep the microwave frequency $f_{\mathrm{mw}} = 2.381$ GHz matching the minimum f_{q}. And the microwave burst time t_{d} is changed to observe the Rabi oscillation. Figure 2(a) displays $\mathrm{d}I/\mathrm{d}V_{\mathrm{D5}}$ as a function of t_{d} and ε with a fixed output microwave amplitude $V_{\mathrm{mw}} = 40$ mV. $\mathrm{d}I/\mathrm{d}V_{\mathrm{D5}}$ changes as t_{d} varies, which indicates a coherent oscillation between states $|0\rangle$ and $|1\rangle$. At $\varepsilon = 41.5$ μeV (marked by the green dashed line), $f_{\mathrm{mw}} = f_{\mathrm{q}}$, the relevant oscillation corresponds to the qubit rotating around the X-axis on the Bloch sphere. The $\mathrm{d}I/\mathrm{d}V_{\mathrm{D5}}$ oscillates at a frequency f_{R} of ~ 160 MHz as shown in the inset of Fig. 2(a). We fit the data with the function $A\exp[-(t_{\mathrm{d}} - t_0)^2/T_2^{\mathrm{R}2}]\cos(2\pi f_{\mathrm{R}} t_{\mathrm{d}} + \theta)$, where T_2^{R} is the coherence time of the Rabi oscillation.[34] The fitted red curve shows good agreement with the experimental data, yielding $T_2^{\mathrm{R}} \approx 14.3$ ns. The extracted T_2^{R} is much longer than the

value obtained in the common charge qubit,[15,17] which benefits from the quasiparallel energy levels and the different spin symmetries of the two states.[24] Furthermore, we increase the microwave amplitude $V_{\rm mw}$ and study its influence on the oscillation frequency $f_{\rm R}$, and the result is displayed in Fig. 2(b). It is observed that the extracted $f_{\rm R}$ increases linearly with $V_{\rm mw}$, which is consistent with the theory.[10,22] At $V_{\rm mw} = 120$ mV, $f_{\rm R}$ reaches ~ 422 MHz, which means that the qubit only takes 0.59 ns to rotate $\pi/2$ around the X-axis (denoted as $X_{\pi/2}$ rotation). The achieved Rabi frequency is much faster than that in typical spin qubits,[5,8–10] and is the highest for hybrid qubit (see Table A1 in Appendix A for more details).

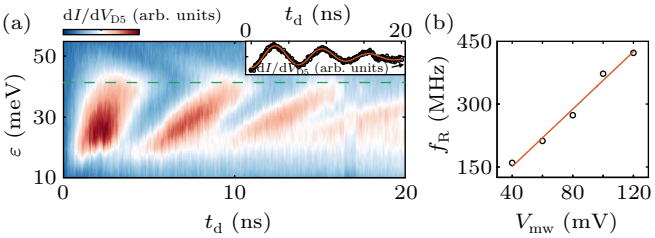


Fig. 2. (a) The Rabi oscillation obtained by measuring dI/dV_{D5} as a function of microwave pulse duration time t_d and detuning ε at microwave amplitude $V_{mw} = 40$ mV and frequency $f_{mw} = 2.381$ GHz. The inset shows the measured dI/dV_{D5} (black dots) as a function of t_d at $\varepsilon = 41.5$ μeV marked by the green dashed line. We fit the data with a Gaussian damped cosine function (red line) and extract the oscillation frequency $f_R \approx 160$ MHz and coherence time $T_2^R \approx 14.3$ ns. (b) The extracted f_R as a function of V_{mw} with fixed $f_{mw} = 2.381$ GHz at $\varepsilon = 41.5$ μeV. At each V_{mw}, we measure the Rabi oscillation and extract f_R from the curve fitting as mentioned above. The red line is a linear fit.[10,22]

The Rabi oscillation frequency and coherence time characterize the property of the driven qubit. Next, we investigate the free evolution of the qubit (i.e., Z-rotation on the Bloch sphere) by performing the Ramsey fringe experiment. As illustrated by the pulse sequence in Fig. 3(a), by implementing the first $X_{\pi/2}$ rotation after the initialization, the qubit is prepared into a superposition state in the X–Y plane. Then during the evolution time t_e, the qubit rotates around the Z-axis at a frequency of f_q. Finally, the qubit is measured after a second $X_{\pi/2}$ rotation. Figure 3(b) shows the resulting Ramsey fringe. In the upper panel, the decay rate of the Ramsey fringes presents a dependence on ε. Around $\varepsilon = 41.5$ μeV (the green dashed line), the amplitude of the fringe decays slowest. To quantitatively study the dependence, we need to extract the decoherence time of the fringes during the free evolution, which is termed as inhomogeneous dephasing time T_2^*. For example, the lower panel of Fig. 3(b) shows the cut at $\varepsilon = 41.5$ μeV. By fitting the data with a Gaussian damped cosine function, T_2^* is estimated to be ~ 5.8 ns. This is smaller compared to the aforementioned T_2^R, since the influence of noise can be suppressed when the qubit is driven.[5,35] With the same processing procedure, we can obtain T_2^* at various ε. Figure 3(c) shows the inhomogeneous dephasing rate $\Gamma_2^* = 1/T_2^*$ as a function of ε, which stems from the quasiparallel energy levels. We overlay the calculated $|\partial f_q/\partial\varepsilon|$ in the figure with a blue line. The trend of Γ_2^* on ε shows a positive correlation with $|\partial f_q/\partial\varepsilon|$, which agrees with the above discussion. Since ε fluctuates in the presence of noise, if $|\partial f_q/\partial\varepsilon|$ is small, f_q changes little.[12,26,33] Therefore, the qubit is more resilient to noise. The presented results suggest that Γ_2^* can be minimized via ε, that is, we can feasibly optimize T_2^* with ε by utilizing the quasiparallel energy levels.

By controlling the phase of the applied microwave, we can achieve rotation around an arbitrary axis in the X–Y plane. As illustrated in Fig. 3(a), when we vary the relative phase ϕ of the second microwave, the rotation axis of the qubit changes to the Ω-axis in the X–Y plane. Figure 3(d) shows dI/dV_{D5} as a function of t_e and ϕ. At each t_e, the oscillation signals at $\phi = 0$ and $\phi = \pi$ are always opposite, which indicates two opposite rotation axes for two different phases. And when fixing t_e, we find that the oscillation phase can be varied consecutively by adjusting ϕ. All these features suggest the controllability of the rotation axis in the X–Y plane with microwave driving. Together with the X-rotation and Z-rotation, we have demonstrated the entire coherent control of the hybrid qubit.

Dynamical decoupling sequences can be employed to mitigate the influence of dissipation, which helps to improve the qubit coherence.[5,36] For example, the Hahn echo refocuses the coherent phase by inserting a X_π rotation during the free evolution,[33,37,38] as schematically shown in Fig. 4(a). The low-frequency noise can be averaged out by the Hahn echo, thereby prolonging the qubit coherence time.[36,39] Here, we implement the Hahn echo sequence in our system. We can change the total evolution time τ and the position of the X_π rotation in the evolution, the latter is parameterized by δt. The upper panel of Fig. 4(b) shows the Hahn echo result as a function of δt and ε while τ is fixed to 5 ns. Moreover, we show the cut at $\varepsilon = 41.5$ μeV in the lower panel. The oscillation frequency is estimated to be 4.81 GHz, which is approximately twice f_q and is consistent with the theoretical prediction.[16,22] When we change the position of the X_π rotation, the oscillation decays slightly as δt deviates from zero where the protective effect of the Hahn echo is optimal. The amplitude at $\delta t = 0$ directly reflects the influence of noise on the qubit decay after the total evolution time τ. This amplitude can be obtained by fitting the oscillation with a Gaussian damped cosine function, as illustrated by the red solid line. We vary τ and perform similar measurements followed by data fitting. Figure 4(c) shows the extracted amplitude as a function of τ. The amplitude decreases monotonically with τ. The red curve is fit to $B\exp[-(\tau-\tau_0)^2/T_2^{e2}]$[16] and yields the echo coherence time $T_2^e \approx 15.0$ ns. This result indicates that the coherence time of the qubit has been improved to ~ 2.6 times the maximum $T_2^* \approx 5.8$ ns by performing the Hahn echo sequence. The good performance of the Hahn echo implies that our qubit is prone to low-frequency noise. Although some works have investigated the coherence performance of the

hybrid qubit,[21,22,24,29,40] the dominant decoherence mechanisms and the noise spectrum have not yet been systematically explored. More work is needed to obtain a deeper understanding of the hybrid qubit and to design appropriate dynamical decoupling sequences for the hybrid qubit to improve the coherence time.[39,41,42]

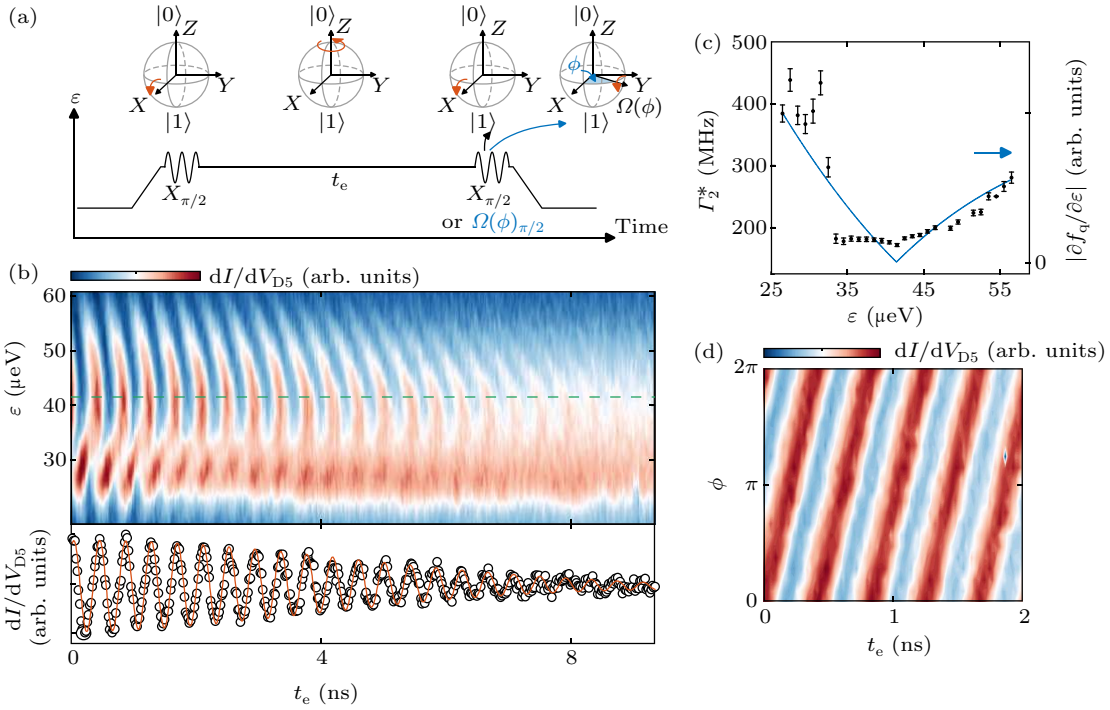


Fig. 3. (a) The pulse sequence used to perform the Ramsey fringe experiment and the axis control in the X–Y plane of the Bloch sphere. The red arrows schematically show the qubit evolution in the Bloch sphere at different pulse stages. We can vary the relative phase ϕ of the second applied microwave, which changes the rotation axis to Ω as shown in the rightmost Bloch sphere. (b) The upper panel displays the Ramsey fringe as a function of free evolution time t_e and detuning ε. The lower panel shows dI/dV_{D5} (black dots) as a function of t_e at $\varepsilon = 41.5$ μeV (indicated by the green dashed line). The red curve is a fit to a Gaussian damped cosine function with qubit's transition frequency $f_q \approx 2.38$ GHz and inhomogeneous dephasing time $T_2^* \approx 5.8$ ns. (c) The dephasing rate $\Gamma_2^* = 1/T_2^*$ extracted by curve fitting as a function of ε. The blue line is the $|\partial f_q/\partial\varepsilon|$ calculated from Eq. (1) with the same parameters as used in Fig. 1(d). The large Γ_2^* and uncertainty at lower ε is probably due to the increased sensitivity to noise. (d) The rotation around an arbitrary axis in the X–Y plane of the Bloch sphere. The measured dI/dV_{D5} as a function of t_e and ϕ at $\varepsilon = 41.5$ μeV.

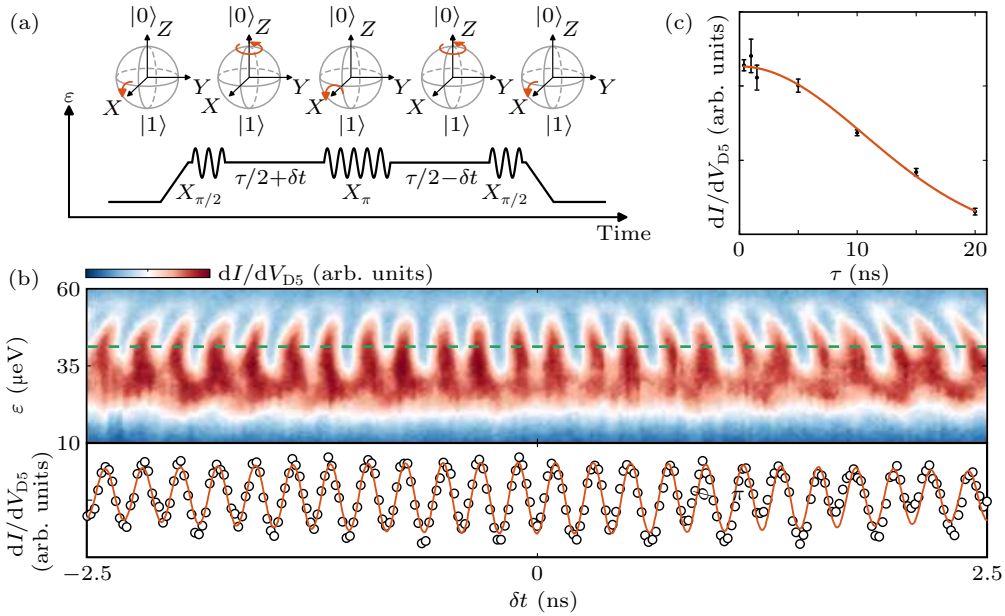


Fig. 4. (a) Schematic of the pulse sequence for the Hahn echo experiment. Similar to Fig. 3(a), the red arrows display the qubit evolution. τ is the total free evolution time. The X_π rotation is performed at $\tau/2 + \delta t$ after the beginning of free evolution. (b) The measured echo result. The upper panel shows dI/dV_{D5} as a function of δt and ε with fixed $\tau = 5$ ns. The cut at $\varepsilon = 41.5$ μeV is plotted in the lower panel. We can extract the oscillation amplitude by fitting the data with a Gaussian damped cosine function. For various τ, we extract the oscillation amplitude at $\varepsilon = 41.5$ μeV and plot the result in panel (c). The red curve represents a fit to a Gaussian damped function with the echo decoherence time $T_2^e \approx 15.0$ ns.[16]

4. Conclusion

In this paper, we demonstrate the coherent manipulation of a tunable hybrid qubit in GaAs using microwave control. In particular, the two lowest energy levels of the presented hybrid qubit are quasiparallel due to the asymmetric and anharmonic potential, which makes the qubit tunable. By performing the Rabi oscillation experiment, we observe the X-rotation with a Rabi coherence time $T_2^{\mathrm{R}} \approx 14.3$ ns, which benefits from the quasiparallelism of energy levels. The maximal Rabi frequency reaches ~ 422 MHz via adjusting the microwave amplitude. These features clearly show the virtue of the hybrid qubit in the coherence compared to the charge qubit and in the manipulation speed compared to the spin qubit. And the Z-rotation is demonstrated in the Ramsey fringe experiment. We find that the quasiparallel energy levels allow the optimization of the inhomogeneous dephasing time by tuning the detuning. In addition, the rotation around an arbitrary axis in the X–Y plane is implemented by controlling the relative phase of the microwave driving. Furthermore, to reduce the influence of low-frequency noise, we exploit the Hahn echo sequence and successfully improve the qubit coherence time $T_2^{\mathrm{e}} \approx 15.0$ ns to a factor of 2.6 compared to the maximum inhomogeneous dephasing time $T_2^* \approx 5.8$ ns. With the qubit's tunability as well as other dynamical decoupling technologies,[39,41,42] we expect further improvement in the qubit coherence time. Our results provide more insight into the tunable hybrid qubit and take a step towards the precise and high-fidelity operation of hybrid qubits with microwave control.

Appendix A: The experimental demonstration of the coherent manipulation of the hybrid qubit

In this section, we collect the experiments for implementing the coherent manipulation of the hybrid qubit, and list the relevant parameters in Table A1.

Table A1. The experimental demonstration of hybrid qubits. For the X-control enabled by microwave, the manipulation frequency is the Rabi frequency f_{R} and coherence time is T_2^{R}. The superscript † indicates the value is estimated from the figure shown in the corresponding reference. The – means this parameter is not measured.

Reference	Type	Controlling method	X-rotation		Z-rotation	
			Manipulation frequency	Coherence time	T_2^*	T_2^{e}
Ref. [21]	typical	nonadiabatic pulse	~ 5.2 GHz	~ 2 ns	~ 10 ns	–
Ref. [22]	typical	microwave	~ 100 MHz	~ 33 ns	~ 11 ns	~ 36 ns†
Ref. [26]	typical	microwave	~ 14.07 MHz	~ 1.02 μs	177 ± 9 ns	–
Ref. [29]	typical	microwave	~ 175 MHz†	~ 37 ns	~ 7 ns	–
Ref. [24]	tunable	nonadiabatic pulse	~ 2.43 GHz	~ 8.1 ns	~ 8.3 ns	–

Acknowledgments

Project supported by the National Natural Science Foundation of China (Grant Nos. 92265113, 12074368, and 12034018) and the USTC Tang Scholarship.

References

[1] Zhang X, Li H O, Wang K, Cao G, Xiao M and Guo G P 2018 *Chin. Phys. B* **27** 020305
[2] Zhang X, Li H O, Cao G, Xiao M, Guo G C and Guo G P 2019 *Natl. Sci. Rev.* **6** 32
[3] Wang K, Li H O, Xiao M, Cao G and Guo G P 2018 *Chin. Phys. B* **27** 090308
[4] Chatterjee A, Stevenson P, De Franceschi S, Morello A, de Leon N P and Kuemmeth F 2021 *Nat. Rev. Phys.* **3** 157
[5] Stano P and Loss D 2022 *Nat. Rev. Phys.* **4** 672
[6] Xu Y Q, Gu S S, Lin T, Wang B C, Li H O, Cao G and Guo G P 2023 *Sci. China Phys. Mech.* **66** 237301
[7] Petta J R, Johnson A C, Taylor J M, Laird E A, Yacoby A, Lukin M D, Marcus C M, Hanson M P and Gossard A C 2005 *Science* **309** 2180
[8] Veldhorst M, Hwang J C C, Yang C H, Leenstra A W, de Ronde B, Dehollain J P, Muhonen J T, Hudson F E, Itoh K M, Morello A and Dzurak A S 2014 *Nat. Nanotechnol.* **9** 981
[9] Kawakami E, Scarlino P, Ward D R, Braakman F R, Savage D E, Lagally M G, Friesen M, Coppersmith S N, Eriksson M A and Vandersypen L M K 2014 *Nat. Nanotechnol.* **9** 666
[10] Yoneda J, Takeda K, Otsuka T, Nakajima T, Delbecq M R, Allison G, Honda T, Kodera T, Oda S, Hoshi Y, Usami N, Itoh K M and Tarucha S 2018 *Nat. Nanotechnol.* **13** 102
[11] Petta J R, Johnson A C, Marcus C M, Hanson M P and Gossard A C 2004 *Phys. Rev. Lett.* **93** 186802
[12] Petersson K D, Petta J R, Lu H and Gossard A C 2010 *Phys. Rev. Lett.* **105** 246804
[13] Dovzhenko Y, Stehlik J, Petersson K D, Petta J R, Lu H and Gossard A C 2011 *Phys. Rev. B* **84** 161302
[14] Cao G, Li H O, Tu T, Wang L, Zhou C, Xiao M, Guo G C, Jiang H W and Guo G P 2013 *Nat. Commun.* **4** 1401
[15] Shi Z, Simmons C B, Ward D R, Prance J R, Mohr R T, Koh T S, Gamble J K, Wu X, Savage D E, Lagally M G, Friesen M, Coppersmith S N and Eriksson M A 2013 *Phys. Rev. B* **88** 075416
[16] Kim D, Ward D R, Simmons C B, Gamble J K, Blume-Kohout R, Nielsen E, Savage D E, Lagally M G, Friesen M, Coppersmith S N and Eriksson M A 2015 *Nat. Nanotechnol.* **10** 243
[17] Li H O, Cao G, Yu G D, Xiao M, Guo G C, Jiang H W and Guo G P 2015 *Nat. Commun.* **6** 7681
[18] Shi Z, Simmons C B, Prance J R, Gamble J K, Koh T S, Shim Y P, Hu X, Savage D E, Lagally M G, Eriksson M A, Friesen M and Coppersmith S N 2012 *Phys. Rev. Lett.* **108** 140503
[19] Koh T S, Gamble J K, Friesen M, Eriksson M A and Coppersmith S N 2012 *Phys. Rev. Lett.* **109** 250503
[20] Shi Z, Simmons C B, Ward D R, Prance J R, Wu X, Koh T S, Gamble J K, Savage D E, Lagally M G, Friesen M, Coppersmith S N and Eriksson M A 2014 *Nat. Commun.* **5** 3020
[21] Kim D, Shi Z, Simmons C B, Ward D R, Prance J R, Koh T S, Gamble J K, Savage D E, Lagally M G, Friesen M, Coppersmith S N and Eriksson M A 2014 *Nature* **511** 70
[22] Kim D, Ward D R, Simmons C B, Savage D E, Lagally M G, Friesen M, Coppersmith S N and Eriksson M A 2015 *NPJ Quantum Inf.* **1** 15004
[23] Wong C H 2016 *Phys. Rev. B* **93** 035409
[24] Cao G, Li H O, Yu G D, Wang B C, Chen B B, Song X X, Xiao M, Guo G C, Jiang H W, Hu X and Guo G P 2016 *Phys. Rev. Lett.* **116** 086801
[25] Wang B C, Cao G, Li H O, Xiao M, Guo G C, Hu X, Jiang H W and Guo G P 2017 *Phys. Rev. Appl.* **8** 064035

[26] Thorgrimsson B, Kim D, Yang Y C, Smith L W, Simmons C B, Ward D R, Foote R H, Corrigan J, Savage D E, Lagally M G, Friesen M, Coppersmith S N and Eriksson M A 2017 *NPJ Quantum Inf.* **3** 32

[27] Frees A, Mehl S, Gamble J K, Friesen M and Coppersmith S N 2019 *NPJ Quantum Inf.* **5** 73

[28] Yang Y C, Coppersmith S N and Friesen M 2020 *Phys. Rev. A* **101** 012338

[29] Jang W, Cho M K, Jang H, Kim J, Park J, Kim G, Kang B, Jung H, Umansky V and Kim D 2021 *Nano Lett.* **21** 4999

[30] Yang Y C, Coppersmith S N and Friesen M 2019 *Phys. Rev. A* **100** 022337

[31] DiCarlo L, Lynch H J, Johnson A C, Childress L I, Crockett K, Marcus C M, Hanson M P and Gossard A C 2004 *Phys. Rev. Lett.* **92** 226801

[32] Chen M B, Jiang S L, Wang N, Wang B C, Lin T, Gu S S, Li H O, Cao G and Guo G P 2021 *Phys. Rev. Appl.* **15** 044045

[33] Dial O E, Shulman M D, Harvey S P, Bluhm H, Umansky V and Yacoby A 2013 *Phys. Rev. Lett.* **110** 146804

[34] Ito T, Otsuka T, Nakajima T, Delbecq M R, Amaha S, Yoneda J, Takeda K, Noiri A, Allison G, Ludwig A, Wieck A D and Tarucha S 2018 *Appl. Phys. Lett.* **113** 093102

[35] Huang Z, Mundada P S, Gyenis A, Schuster D I, Houck A A and Koch J 2021 *Phys. Rev. Appl.* **15** 034065

[36] Paladino E, Galperin Y M, Falci G and Altshuler B L 2014 *Rev. Mod. Phys.* **86** 361

[37] Koppens F H L, Nowack K C and Vandersypen L M K 2008 *Phys. Rev. Lett.* **100** 236802

[38] Vandersypen L M K and Chuang I L 2005 *Rev. Mod. Phys.* **76** 1037

[39] Alvarez G A, Ajoy A, Peng X and Suter D 2010 *Phys. Rev. A* **82** 042306

[40] Ferraro E, Fanciulli M and De Michielis M 2018 *Adv. Quantum Technol.* **1** 1800040

[41] Bluhm H, Foletti S, Neder I, Rudner M, Mahalu D, Umansky V and Yacoby A 2011 *Nat. Phys.* **7** 109

[42] Malinowski F K, Martins F, Nissen P D, Barnes E, Cywiński Ł, Rudner M S, Fallahi S, Gardner G C, Manfra M J, Marcus C M and Kuemmeth F 2017 *Nat. Nanotechnol.* **12** 16